Entropically damped form of artificial compressibility for explicit simulation of incompressible flow

Jonathan R. Clausen*
Sandia National Laboratories, Albuquerque, New Mexico 87185, USA
(Received 15 February 2012; published 28 January 2013)

An alternative artificial compressibility (AC) scheme is proposed to allow the explicit simulation of the incompressible Navier-Stokes (INS) equations. Traditional AC schemes rely on an artificial equation of state that gives the pressure as a function of the density, which is known to enforce isentropic behavior. This behavior is nonideal, especially in viscously dominated flows. An alternative, the entropically damped artificial compressibility (EDAC) method, is proposed that employs a thermodynamic constraint to damp the pressure oscillations inherent to AC methods. The EDAC method converges to the INS in the low-Mach limit, and is consistent in both the low- and high-Reynolds-number limits, unlike standard AC schemes. The proposed EDAC method is discretized using a simple finite-difference scheme and is compared with traditional AC schemes as well as the lattice-Boltzmann method for steady lid-driven cavity flow and a transient traveling-wave problem. The EDAC method is shown to be beneficial in damping pressure and velocity-divergence oscillations when performing transient simulations. The EDAC method follows a similar derivation to the kinetically reduced local Navier-Stokes (KRLNS) method [Borok *et al.*, Phys. Rev. E **76**, 066704 (2007)]; however, the EDAC method does not rely on the grand potential as the thermodynamic variable, but instead uses the more common pressure-velocity system. Additionally, a term neglected in the KRLNS is identified that is important for accurately approximating the INS equations.

DOI: 10.1103/PhysRevE.87.013309 PACS number(s): 47.11.Bc

I. INTRODUCTION

Fluid flows can be broadly split into two regimes: compressible and incompressible. In the former case, compressibility effects are important, and the equations governing the flow include mass conservation, momentum conservation, a thermodynamic equation of state, and energy conservation (or entropy balance). These equations are collectively referred to as the compressible Navier-Stokes (CNS) equations. Compressibility effects are governed by the Mach number $\mathrm{Ma} \equiv u_0/c_s$, where u_0 is the flow velocity and c_s is the speed of sound. Time scales of interest include the acoustic time scale $t_a \sim L/c_s$, where L is a length scale of interest, the diffusive time scale $t_d \sim L^2/\nu$, where ν is the fluid kinematic viscosity, and the convective time scale $t_c \sim L/u_0$. In the limit $\mathrm{Ma} \to 0$, the acoustic time scale becomes singularly perturbed, i.e., acoustic pressure disturbances are transmitted instantaneously. The conservation of mass requirement reduces to the well-known incompressibility requirement

$$\nabla \cdot \boldsymbol{u} = 0, \tag{1}$$

which, when combined with the equations governing the conservation of momentum, yields the incompressible Navier-Stokes (INS) equations. In these equations, the thermodynamic state becomes fixed, thus the energy equation is decoupled from the momentum equation and incompressibility requirement. This system represents a considerable simplification compared with the traditional CNS equations. At low-Mach numbers, the simulations using the CNS equations become difficult due to the disparity between the acoustic and convective wave speeds. The strict decoupling of the energy equation found in the INS can be weakened somewhat via an acoustic filtering procedure that separates the pressure into mechanical and thermodynamic parts, thus yielding a temperature-only equation of state for the thermodynamic pressure [1]. These equations allow for a temperature-dependent density and are typically used in cases where flow-driven compressibility effects are negligible; however, temperature gradients can create large density gradients that cannot be adequately described via a Boussinesq approximation.

Despite the reduced system, significant computational complexity is associated with solving the INS equations using numerical techniques. Owing to the instantaneous propagation of information associated with the singularly perturbed acoustic wave velocity, communication loads are typically high in parallel computing applications, making scalability on massively parallel computers nontrivial. Traditional solution techniques often rely on fractional step approaches. A broad class of these methods has been developed based on a Hodge decomposition of the velocity field, pioneered with the original projection methods of Chorin [2,3]. These methods rely on some variation of operator splitting [4,5] to decompose the problem into several steps, which can often be generalized as the following: a velocity update to a intermediate value, application of an incompressibility constraint, and a velocity correction step to maintain a solenoidal velocity field. Original formulations of the projection schemes satisfied the incompressibility constraint discretely; however, more recent formulations have favored approximate forms that only satisfy the discrete divergence to the numerical accuracy of the method [6–8]. This point is important, since although the equations associated with projection methods may be strictly incompressible, the discrete solution will contain numerical errors resulting in some degree of compressibility. The form of the incompressibility constraint is typically formed using the pressure-Poisson form of the continuity equation, which is elliptic and thus requires an iterative approach to solving it. A more detailed review on projection-based methods can be found in Brown *et al.* [8].

*jclause@sandia.gov

In general, scientific computational resources are trending towards increasingly parallel architectures, with next generation "exascale" supercomputers having in excess of a million processing cores [9]. This trend is being accelerated by the emergence of general-purpose processing on graphic processor units (GPGPU) as a viable resource for scientific computing. GPGPU are exceedingly powerful; for comparison, an Intel Xeon X5680 (Westmere) processor has a peak performance of 160 giga floating-point operations per second (GFLOPS), while a NVIDIA Tesla 2050 (Fermi) GPU has a peak performance of 1180 GFLOPS [10]. This massive performance is in large part due to the increased parallelism present in GPUs. As computational resources trend towards evermore parallel architectures, algorithms which are capable of scaling on these resources are desirable.

In the context of incompressible flows, an explicit and local procedure has the potential to leverage these increasingly parallel computational resources. Removing the pressure-Poisson solve requires weakening the constraint of strict incompressibility and looking instead at the limit of incompressibility, with this class of methods being broadly referred to as pseudocompressible. This strategy was taken very early in the simulation of fluid flows by Chorin [11], in which an artificial equation of state is prescribed in a method referred to as artificial compressibility (AC). This equation of state is equivalent to the isentropic limit (see Sec. II), with compressibility relegated to $O(\mathrm{Ma}^2)$ effects. In this method, the Mach number becomes an artificial parameter, which may be larger than the physical Mach number, yet small enough to ensure negligible compressibility errors. This method was originally conceived as a means to iterate towards a steady solution, and many authors have noted issues with performing time-accurate solutions unless a dual-time-stepping iterative procedure is used [12–15], although some evidence exists that with a sufficiently small Mach number, time-accurate solutions are feasible [16,17]. Perhaps the most successful pseudocompressible computational method is the lattice-Boltzmann (LB) method [18,19]. This method is based on a simplified kinetic model of the continuum governing equations; however, the key to its success as a massively parallel and scalable method lies in the finite, but large, sound speed.

In the classic AC method of Chorin, an artificial equation of state is provided; however, this artificial equation of state is equivalent to providing an additional thermodynamic constraint. This additional constraint is necessary to eliminate the energy or entropy equation from the compressible Navier-Stokes (CNS), reducing the number of equations and unknowns by one. The traditional AC method of Chorin is isentropic, thus the constraint equation is $ds = 0$, where s is the specific entropy. Although the CNS behave isentropically in the strict incompressible limit ($\mathrm{Ma} \to 0$), the traditional isentropic limit is just one potential, and artificial, choice of thermodynamic constraint when considering the higher $O(\mathrm{Ma}^2)$ terms. While this choice may be appropriate on acoustic time scales, at the longer viscous and convective time scales, dissipation is important and the isentropic assumption may not be appropriate.

In this paper, an alternate constraint equation is proposed based on minimizing density fluctuations. Minimizing the density fluctuations results in a thermodynamic relationship constraining changes in pressure to changes in temperature. As discussed in Sec. II, this constraint has several important consequences, and this selection results in markedly reduced pressure fluctuations by introducing a smoothing term into the equation governing the evolution of the pressure. In effect, the acoustic waves are rapidly damped through entropy generation. This contrasts with the isentropic case, where acoustic wave damping occurs strictly through the coupling of the pressure with the momentum equation. The resulting system of equations subject to the above constraint is referred to as the entropically damped artificially compressible (EDAC) Navier-Stokes. Physically, at time scales much larger than t_a, acoustic waves have dissipated viscously, which is not a process that conserves entropy. It is shown in Sec. II that the EDAC equations converge to the INS as $\mathrm{Ma} \to 0$.

This research was in part motivated by a series of papers that also proposed an alternate thermodynamic basis for the limit of incompressibility [20–22], in which the authors noted that an additional smoothing term is beneficial. This research offers the following contributions:

(1) The governing equations are not recast using the thermodynamic grand potential since this substitution complicates the derivation. Instead, the derivation proceeds directly from the CNS in terms of the thermodynamic variables of interest.

(2) The reduced equations in Borok *et al.* [22] are missing an important term, which is identified in Sec. II.

(3) The development of the smoothing or dissipative term is a direct consequence of an artificially chosen thermodynamic relationship. This relationship was chosen in the derivation of Ansumali *et al.* [20] as an approximation, yet is stated unambiguously here as an artificial constraint. Thus, the equations derived in both the EDAC and kinetically reduced local Navier-Stokes (KRLNS) methods do not represent the true thermodynamic limit of incompressibility, but just one potential limit subject to the chosen constraint.

This paper proceeds by closely examining the CNS equations as $\mathrm{Ma} \to 0$ in Sec. II, and the effect of the various thermodynamic constraints used to derive an artificial equation of state. Section III describes a simple finite-difference discretization method used to explore the performance and accuracy of the EDAC method. Then, Sec. IV shows some simulations of the EDAC method for lid-driven cavity, traveling-wave, and shear-layer flows. The results are compared with those of classical AC and LB methods. Section V discusses the findings and places them in the context of future developments.

II. THERMODYNAMIC LIMIT OF INCOMPRESSIBILITY

In order to study the behavior of the CNS in the limit of incompressibility, the CNS equations are made dimensionless. Consequently, there are several dimensionless parameters of interest: The Prandtl number is defined as $\mathrm{Pr} \equiv \mu c_p / k$, where μ is the fluid shear viscosity, c_p is the specific heat at constant pressure, and k is the thermal conductivity. The Reynolds number is defined as $\mathrm{Re} \equiv \rho_0 u_0 L / \mu$, where ρ_0 and L are a characteristic density and length, respectively. The ratio of specific heats is defined as $\gamma \equiv c_p / c_v$, where c_v is the specific heat at constant volume. Note that all material properties are assumed constant including the fluid viscosity.

The variables are scaled according to

$$\rho^* = \rho/\rho_0, \quad \boldsymbol{u}^* = \boldsymbol{u}/u_0, \quad T^* = \frac{T - T_0}{\mathrm{Pr}\, u_0^2/c_p},$$
$$s^* = \frac{s}{c_p}, \quad P^* = \frac{P - P_0}{\rho_0 u_0^2},$$

where starred quantities are dimensionless, and P_0 and T_0 are a chosen reference pressure and temperature, respectively. Dropping the starred notation hereafter, and assuming all quantities are dimensionless unless otherwise noted, the continuity and momentum equations of the CNS can be written as [23]

$$\frac{1}{\rho}\frac{D\rho}{Dt} = -\nabla \cdot \boldsymbol{u}, \tag{2}$$

$$\rho \frac{D\boldsymbol{u}}{Dt} = -\nabla P + \frac{1}{\mathrm{Re}}\nabla \cdot \boldsymbol{\tau}, \tag{3}$$

where $\boldsymbol{\tau}$ is the viscous stress tensor, and the convective derivative is defined as

$$\frac{D(\cdot)}{Dt} \equiv \frac{\partial(\cdot)}{\partial t} + \boldsymbol{u} \cdot \nabla(\cdot).$$

The continuity and momentum equations are augmented by a thermodynamic equation expressing entropy balance (or, alternately, energy conservation). Taking a standard form for entropy balance [23] and rendering dimensionless via the above scaling yields

$$\left(\frac{\mathrm{Pr}\gamma \mathrm{Ma}^2}{A} T + 1\right)\rho \frac{Ds}{Dt} = \frac{\mathrm{Ma}^2\gamma}{A}\frac{1}{\mathrm{Re}}(\nabla^2 T + \Phi), \tag{4}$$

where Φ is the viscous dissipation. Here $A \equiv \alpha\rho_0 c_p T_0$ is an additional dimensionless parameter, where α is the isothermal compressibility coefficient. Also, Fourier's heat flux constitutive relation has been used to simplify the heat flux. Note that only two thermodynamic variables are independent, e.g., one can express $\rho = \rho(P,s)$ and $T = T(P,s)$ to ensure the system described by (2)–(4) is complete.

The above system can be simplified by expanding the density in terms of its thermodynamic relationship,

$$d\rho = \mathrm{Ma}^2 dP - B\left(\frac{\mathrm{Pr}\gamma \mathrm{Ma}^2}{A} T + 1\right)\rho ds, \tag{5}$$

where $B \equiv \beta T_0$, β is the thermal expansion coefficient, and γ is the ratio of specific heats. Next, taking the time derivative of Eq. (5) and combining the result with the continuity (2) and thermodynamic conservation (4) equations results in

$$-\rho\nabla \cdot \boldsymbol{u} = \mathrm{Ma}^2 \frac{DP}{Dt} - \frac{\mathrm{Ma}^2\gamma}{\mathrm{Re}}\frac{B}{A}(\nabla^2 T + \Phi). \tag{6}$$

The reduced equations given in Eqs. (6) and (3) do not represent a complete system since the number of unknowns (two thermodynamic and three momentum) is greater than the number of equations (four). An additional thermodynamic constraint is necessary to complete the system. Equation (6) can also be derived by combining the continuity equation, the thermal energy equation, and the thermodynamic relationship for the density with pressure and temperature as the independent thermodynamic variables; however, the derivation from the entropy form is more convenient.

A. Isentropic limit

One potential option to close the above system is to assume isentropic behavior, i.e., $ds = 0$. With the isentropic assumption, (6) becomes

$$\frac{DP}{Dt} = -\frac{1}{\mathrm{Ma}^2}\rho\nabla \cdot \boldsymbol{u}. \tag{7}$$

Two approximations can be made: First, the convective derivative can be approximated such that $DP/Dt \approx \partial P/\partial t$ due to the much faster velocity of the acoustic waves relative to the convective velocity. Second, the density perturbations are given as $\rho \approx 1 + O(\mathrm{Ma}^2)$, thus the higher-order terms involving the density can be neglected. The resulting update for the pressure is

$$\frac{\partial P}{\partial t} = -\frac{1}{\mathrm{Ma}^2}\nabla \cdot \boldsymbol{u}. \tag{8}$$

This result is equivalent to the classical AC methods, which are commonly motivated by assuming the artificial equation of state $\rho = \mathrm{Ma}^2 P$. While entropy balance (4) shows isentropic behavior to $O(\mathrm{Ma}^2)$, (6) clearly shows that both the pressure and entropic contributions contain terms of the same order. This behavior suggests that an isentropic assumption, while certainly valid to $O(\mathrm{Ma}^2)$, may not be the only acceptable choice for a pressure update procedure.

B. Minimization of density fluctuations

As an alternative constraint, one can try to artificially suppress fluctuations in density *separately* from the low-Mach limiting process. Consider the thermodynamic function for the density as a function of the pressure and temperature,

$$\frac{d\rho}{\rho} = \gamma \mathrm{Ma}^2\left(dP - \frac{\mathrm{Pr}B}{A} dT\right). \tag{9}$$

It is apparent that driving the term in parentheses towards zero will limit the fluctuations in density caused by changes in the thermodynamic state, which suggests a thermodynamic relationship of the form

$$dP \approx \frac{\mathrm{Pr}B}{A} dT, \tag{10}$$

which can be used to eliminate the temperature diffusion term in Eq. (6). This relationship is identical to that used in Ansumali *et al.* [20]. It is important to realize that while the density naturally becomes constant in the low-Mach-number limit for a given material region, (10) represents an additional constraint that minimizes changes in density by thermodynamically constraining fluctuations in temperature to fluctuations in pressure. This constraint is entirely artificial, but so is the isentropic constraint, and, as is shown in Sec. IV, this constraint yields several desirable properties.

Simplifying (6) using (10) gives

$$\frac{DP}{Dt} = -\frac{1}{\mathrm{Ma}^2}\rho\nabla \cdot \boldsymbol{u} + \frac{\gamma}{\mathrm{PrRe}}\nabla^2 P + \frac{B}{A}\frac{\gamma}{\mathrm{Re}}\Phi. \tag{11}$$

For the subsequent investigation of Eq. (11), several simplifications are made. The density is eliminated just as in the isentropic case, $\mathrm{Pr} = \gamma$, and the effects of viscous dissipation are neglected. These simplifications are possible through

the appropriate selection of the dimensionless parameters, although certainly not required. The resulting simplified version is shown as

$$\frac{DP}{Dt} = -\frac{1}{\mathrm{Ma}^2}\nabla\cdot\boldsymbol{u} + \frac{1}{\mathrm{Re}}\nabla^2 P, \tag{12}$$

which, when combined with the momentum equation (3), forms a complete system for the solution of pseudocompressible flow that is referred to as the EDAC method. In this method, acoustic pressure waves are effectively damped through an entropy-generation mechanism that is a result of the constraint given in Eq. (10).

C. Discussion

Several points of discussion are appropriate. First, consider the behavior of the AC and EDAC methods at varying limits. As $\mathrm{Ma}\to 0$, both methods converge to the INS with $O(\mathrm{Ma}^2)$ errors. As the viscous terms become less important, i.e., $\mathrm{Re}\to\infty$, the EDAC and AC methods converge to the same isentropic behavior. Physically, this behavior is consistent because at high Reynolds number, (4) shows a convergence to isentropic behavior. The primary difference occurs in the viscously dominated regime as $\mathrm{Re}\to 0$. In this case, the EDAC method converges to the pressure-Poisson equation for Stokes flow,

$$\nabla^2 P = 0, \tag{13}$$

which also identically enforces incompressibility. In contrast, the AC method is unaffected by the choice of Reynolds number and is solely dependent on the low-Mach limiting process to achieve incompressible behavior. The ability of the EDAC to demonstrate proper behavior at both the viscous and inertial limits is the key to developing a time-accurate AC method.

It is also worth comparing the EDAC method with the existing KRLNS method. The KRLNS method is based on a substitution,

$$\mathcal{G} = P - e_k, \tag{14}$$

where $\mathcal{G}$ is stated to be the negative of the grand potential, and $e_k \equiv \rho\boldsymbol{u}\cdot\boldsymbol{u}/2$ is the kinetic energy. After simplifying the CNS using the above substitution, an update procedure is obtained for $\mathcal{G}$ as [22]

$$\frac{\partial\mathcal{G}}{\partial t} = -\frac{1}{\mathrm{Ma}^2}\nabla\cdot\boldsymbol{u} + \frac{1}{\mathrm{Re}}\nabla^2\mathcal{G}. \tag{15}$$

Taking the EDAC equation (12) and subtracting (15), in conjunction with the definition for $\mathcal{G}$, reveals a difference, which is shown as

$$\mathrm{EDAC}-\mathrm{KRLNS} = \nabla\cdot(\boldsymbol{u}e_k) + \frac{1}{\mathrm{Re}}\nabla\boldsymbol{u}:\nabla\boldsymbol{u}. \tag{16}$$

The first term on the right-hand side is associated with the convection of kinetic energy and is likely negligible based on the difference in acoustic and convective speeds. The second term, however, is important in obtaining a qualitatively correct pressure evolution, as shown in Sec. IV. Although both of these terms are missing in the reduced set of equations [22], they are present in earlier formulations (cf. Eq. (10) in Ansumali *et al.* [20]).

In all derivations of the KRLNS [20–22], a key simplification relates fluctuations in temperature to fluctuations in the grand potential, which is based on the argument that at long time scales, the density is approximately constant. This assumption requires the thermodynamic constraint shown in Eq. (10); consequently, the KRLNS equations and likewise the EDAC equations (12) represent only one potential limit of incompressibility subject to the previously mentioned thermodynamic constraint.

III. NUMERICAL METHOD

In order to study the numerical behavior of the EDAC equations and compare the results with traditional AC and LB techniques, the equations are discretized using a simple MacCormack finite-difference scheme [24]. The MacCormack scheme is a predictor-corrector scheme with a nominal accuracy of $O(\Delta x^2,\Delta t^2)$. Restating the governing equations in conservative form for a two-dimensional system gives

$$\frac{\partial\boldsymbol{U}}{\partial t} + \frac{\partial\boldsymbol{F}(\boldsymbol{U})}{\partial x} + \frac{\partial\boldsymbol{G}(\boldsymbol{U})}{\partial y} = \boldsymbol{S}(\boldsymbol{U}), \tag{17}$$

where $\boldsymbol{U}\equiv(P,\boldsymbol{u})$ is a vector of the solution variables. The functions $\boldsymbol{F}$ and $\boldsymbol{G}$ capture advection terms, and $\boldsymbol{S}$ contains the source terms. Note that in writing the EDAC equations in conservative terms, we neglected higher-order terms of $\nabla\cdot\boldsymbol{u}$ in Eq. (12) and the bulk viscosity component of the viscous stress tensor.

The MacCormack discretization of the left-hand side of Eq. (17) gives a predictor-corrector sequence of

$$\boldsymbol{U}^*_{i,j} = \boldsymbol{U}^n_{i,j} - \frac{\Delta t}{\Delta x}\left(\boldsymbol{F}^n_{i+1,j}-\boldsymbol{F}^n_{i,j}\right) - \frac{\Delta t}{\Delta y}\left(\boldsymbol{G}^n_{i,j+1}-\boldsymbol{G}^n_{i,j}\right) + \boldsymbol{S}(\boldsymbol{U}^n) \tag{18}$$

$$\boldsymbol{U}^{n+1}_{i,j} = \frac{1}{2}\left\{\boldsymbol{U}^n_{i,j} + \boldsymbol{U}^*_{i,j} - \frac{\Delta t}{\Delta x}(\boldsymbol{F}^*_{i,j}-\boldsymbol{F}^*_{i-1,j}) - \frac{\Delta t}{\Delta y}[\boldsymbol{G}^*_{i,j}-\boldsymbol{G}^*_{i,j-1}+\boldsymbol{S}(\boldsymbol{U}^*)]\right\}, \tag{19}$$

where n denotes a discrete time and i,j denote a discrete spatial location. Not shown above are the source terms $\boldsymbol{S}(\boldsymbol{U})$, which are evaluated using second-order central differences. As written in Eqs. (18) and (19), the spatial differencing progresses in a forward-back manner. In the presented simulations, the forward-back integration is alternated with a back-forward step to reduce errors [25]. The stability limit of the MacCormack scheme is given in dimensionless form as [25]

$$\Delta t_{\mathrm{CFL}} \leqslant \sigma\left(\frac{1}{\Delta x}+\frac{1}{\Delta y}+\frac{1}{\mathrm{Ma}}\sqrt{\frac{1}{\Delta x^2}+\frac{1}{\Delta y^2}}\right)^{-1}, \tag{20}$$

where σ is a safety factor and is chosen to be $1/2$ in this work. An additional stability limit exists for the diffusion term such that

$$\Delta t_{\mathrm{diff}} \leqslant \frac{\sigma\,\mathrm{Re}}{2}\left(\frac{1}{\Delta x^2}+\frac{1}{\Delta y^2}\right)^{-1}. \tag{21}$$

Stability is ensured by selecting a time step such that $\Delta t = \min(\Delta t_{\mathrm{CFL}},\Delta t_{\mathrm{diff}})$.

Code verification is performed by the method of manufactured solutions (MMS) [26]. The solution form is chosen as a

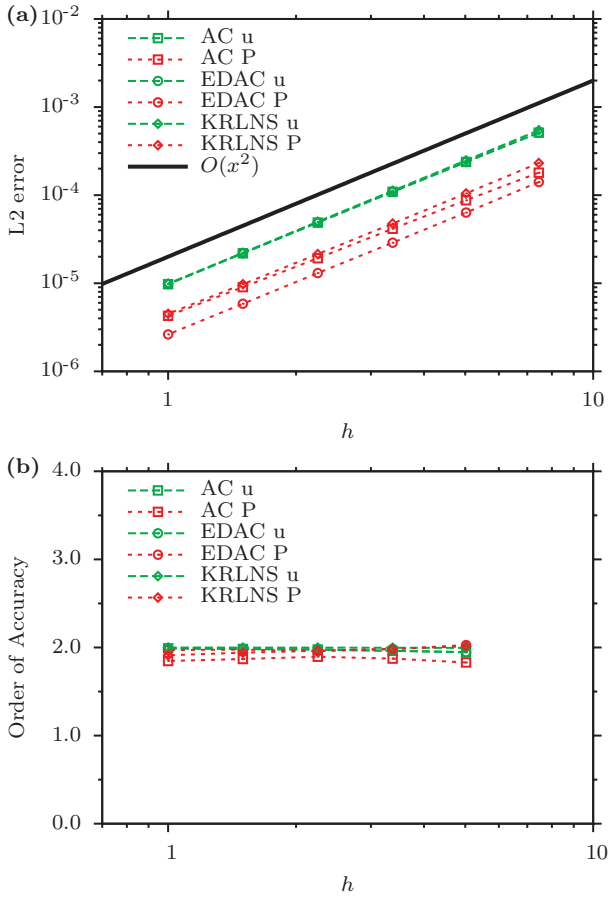

FIG. 1. (Color online) The (a) convergence and (b) order of accuracy plots for the traveling-wave solution using MMS to isolate the discretization errors.

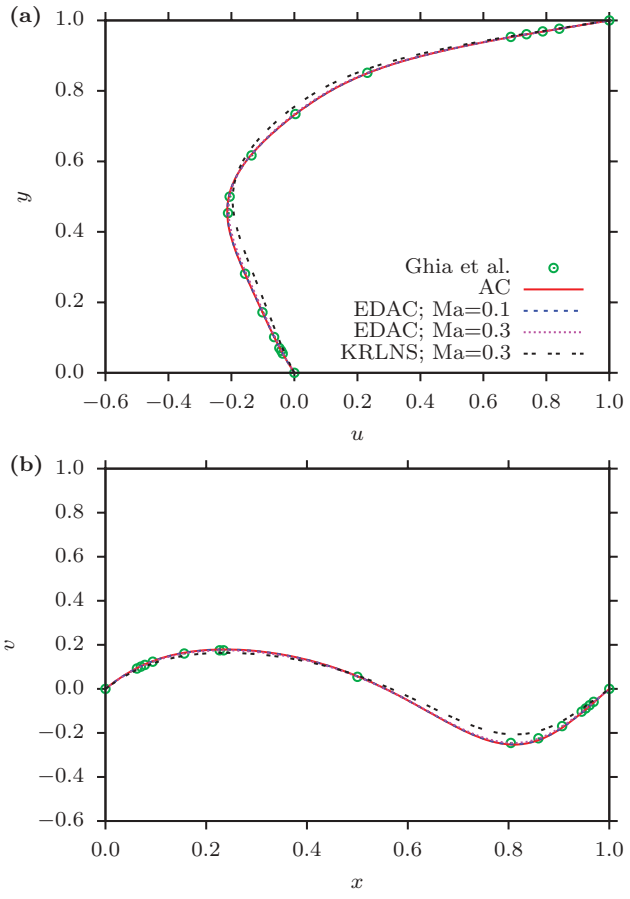

FIG. 2. (Color online) LDCF results for $\mathrm{Re} = 100$ showing excellent agreement for the (a) u and (b) v velocity components.

traveling-wave problem [27], which has an exact solution for the INS shown as

$$u(x,y,t) = \frac{1}{3} + \frac{2}{3}\left\{\cos\left[2\pi\left(x-\frac{t}{3}\right)\right]\sin\left[2\pi\left(y-\frac{t}{3}\right)\right] \times \exp\left(\frac{-8\pi^2 t}{\mathrm{Re}}\right)\right\}, \quad (22)$$

$$v(x,y,t) = \frac{1}{3} - \frac{2}{3}\left\{\sin\left[2\pi\left(x-\frac{t}{3}\right)\right]\cos\left[2\pi\left(y-\frac{t}{3}\right)\right] \times \exp\left(\frac{-8\pi^2 t}{\mathrm{Re}}\right)\right\}, \quad (23)$$

$$P(x,y,t) = -\frac{1}{9}\left\{\cos\left[4\pi\left(x-\frac{t}{3}\right)\right] + \cos\left[4\pi\left(y-\frac{t}{3}\right)\right]\right\} \times \exp\left(\frac{-16\pi^2 t}{\mathrm{Re}}\right), \quad (24)$$

with doubly periodic boundary conditions; however, the AC, KRLNS, and EDAC methods only approximate the INS equations with an error of $O(\mathrm{Ma}^2)$. To remove this error, analytical source terms are derived using a computer algebra program that, when added to Eqs. (8) and (12), make the solution in Eqs. (22)–(24) exact. The full form for these source terms can be found in the Appendix A. Accordingly, errors are restricted to discretization errors. The ability of the various methods to approximate the INS will be discussed in the following section. A grid-refinement study is conducted, where $h = \Delta x/\Delta x_{\mathrm{fine}}$ describes the relative mesh resolution. At all refinements, $\Delta x/\Delta t$ is held constant and the results are shown for the L^2 error norms in Fig. 1(a) and for the order of accuracy in Fig. 1(b). All error norms are calculated at $t = 0.08$. The results in Fig. 1 show the expected nominal quadratic error convergence.

In addition to the finite-difference scheme mentioned above, a simple single-relaxation-time LB method is used [28]. The LB approximates the INS equations in the long-time limit, and relies on solving a discrete version of the Boltzmann equation. The reader is referred to Chen and Doolen [18] and Aidun and Clausen [19] for relevant reviews of the implementation of the LB method. The LB method has been long known to behave similarly to an AC method [16] with an equation of state $P = c_s^2\rho$. The LB method has been quite successful in simulating a variety of flows, including turbulent, suspension, and multiphase flows. The locality of information propagation, i.e., pseudocompressibility, of the method has been key to its scalability, with simulations scaling to $O(100\,000)$ processors [29].

IV. RESULTS

This section demonstrates the ability of the EDAC equations to model the INS equations in both steady and transient

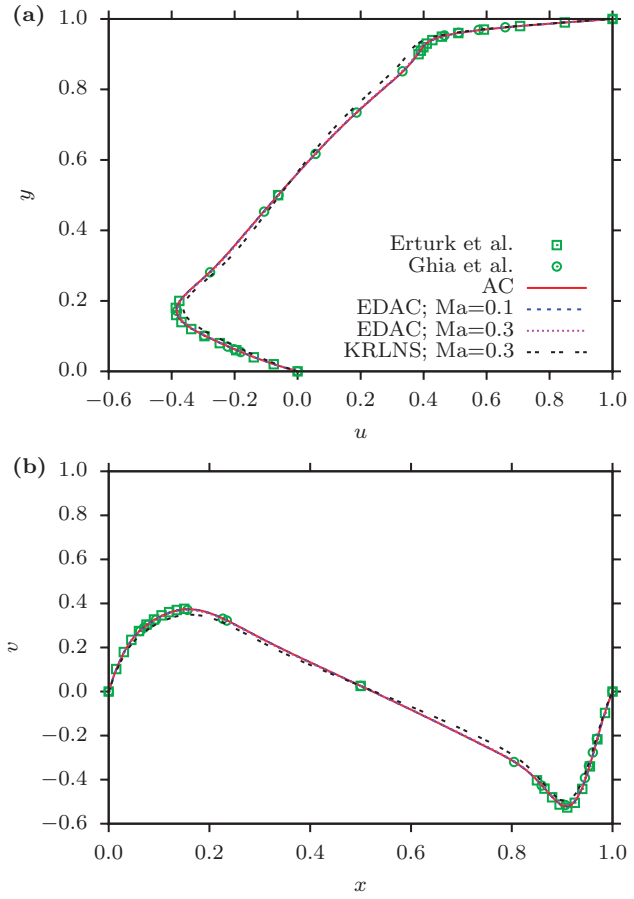

FIG. 3. (Color online) LDCF results for Re = 1000 showing excellent agreement for the (a) u and (b) v velocity components.

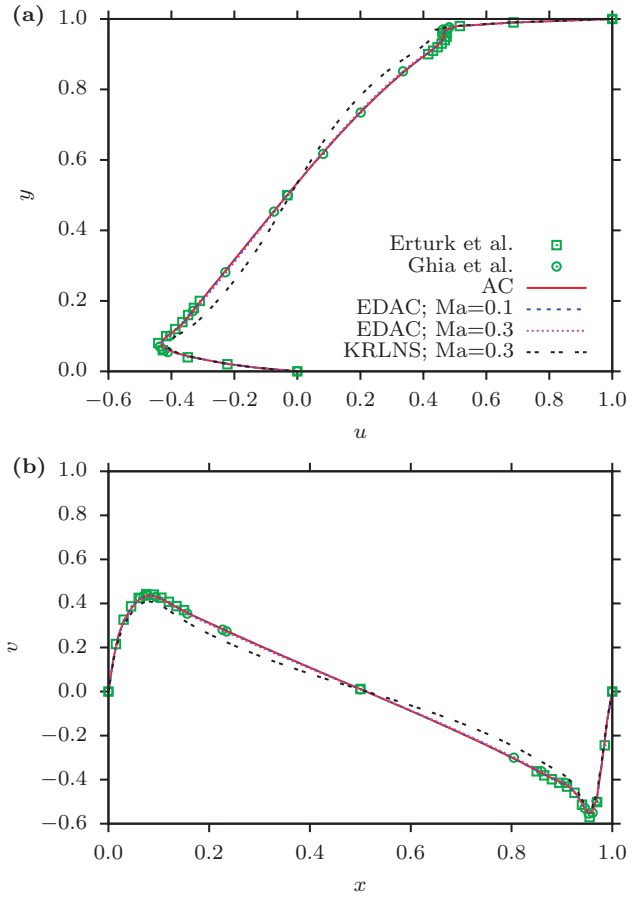

FIG. 4. (Color online) LDCF results for Re = 5000 showing excellent agreement for the (a) u and (b) v velocity components.

flows using the MacCormack finite-difference discretization. Comparisons are made to the traditional AC method, the recently developed KRLNS method, and, where appropriate, the LB method. The results show that both the EDAC and AC methods perform well in the studied lid-driven cavity flow (LDCF). While the AC method is expected to converge to the INS solution at a steady state regardless of the Mach number, the EDAC method shows good agreement even at relatively high-Mach numbers (Ma = 0.3). The traveling-wave problem shows incorrect transient behavior for the AC method unless a very small Mach number is chosen, while the EDAC method agrees well with the analytical solution. The KRLNS method shows errors in both the steady LDCF and transient traveling-wave problems.

A. Lid-driven cavity flow

Lid-driven cavity flow is a canonical flow in the evaluation of incompressible flow solvers due to the complex flow patterns exhibited. For this test case, the simulation domain is a 1×1 square, with the top wall moving to the right with velocity $u_{\text{top}} = 1$. Simulations are performed using three methods (AC, EDAC, and KRLNS) at Re = 100, 1000, and 5000. For the AC method, it is trivial to see that at a steady state, (8) is independent of the Mach number and identical to the INS result; however, for the EDAC and KRLNS methods, an error still remains. Thus, Ma = 0.1 and 0.3 simulations are performed. All simulations are performed on a 256×256 mesh. The velocity profiles are compared with high-resolution stream-vorticity formulations [30,31]. Unlike traditional INS solvers, the pressure evolution equation requires an additional boundary condition. Following Borok *et al.* [22], for the AC, EDAC, and KRLNS simulations, a Neumann condition for the pressure is used enforcing $\partial P/\partial n = 0$, where n is the wall-normal distance. The boundary condition is implemented via a second-order one-sided finite difference. Simulations are considered steady state when the L^2 norms of the unsteady terms are less than 1.0×10^{-8}.

Figure 2 shows the centerline velocity profiles for Re = 100. Excellent agreement is seen between the AC results, the EDAC results up to Ma = 0.3, and the numerical results of Ghia *et al.* [30]. The EDAC and AC results are nearly indistinguishable from one another; however, the KRLNS results show a noticeable deviation. Although the author notes that Ma = 0.3 likely exceeds the Ma $\ll 1$ assumption, differences are seen for lower Mach cases as well [22]. As noted in Borok *et al.* [22], the KRLNS results would improve with a refinement in the Mach number, yet the EDAC method is clearly more accurate at relatively higher Mach numbers. Figure 3 shows the velocity profiles at Re = 1000 and Fig. 4 shows the velocity profiles at Re = 5000. The trends seen at Re = 100 continue, with excellent agreement with the AC and EDAC methods at all Mach numbers simulated. The KRLNS

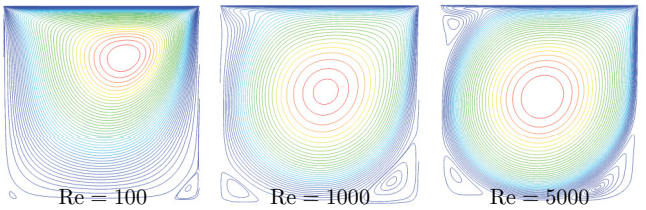

FIG. 5. (Color online) Streamlines from the EDAC simulations at Ma = 0.1 showing the formation of three vortices: the primary, bottom left, and bottom right. At Re = 5000, an additional vortex forms along the top left of the domain, as is expected. Warmer colors indicate higher stream-function values.

method continues to show larger deviations, particularly at the highest Reynolds number. While the error term in Eq. (16) scales 1/Re, larger velocity gradients are present, creating larger errors.

At low Reynolds numbers, three vortices appear during the simulation: a primary vortex located near the center of the domain, and two secondary vortices located in the bottom left and bottom right corners of the simulation domain. For Re = 5000, a vortex appears near the top left corner, and additional vortices are known to form at even higher Reynolds numbers [32]. Streamlines showing the development of the vortices are listed in Fig. 5. The locations of the primary and secondary vortices are shown in Table I and the tertiary vortex location at Re = 5000 is listed in Table II. The following are some comments on the vortex location results: First, for the Re = 100 case, the AC and EDAC cases show large errors in the location and strength of the secondary vortices. These vortices are very weak at this Reynolds number, and the discrepancies are seen in the EDAC as well as the existing AC methods. The errors could be due to the MacCormack discretization, which was chosen as a simple way to explore the behavior of the EDAC method and not for numerical accuracy. Another potential culprit could be the Neumann pressure boundary condition, which is not present in a strictly INS flow. More accurate numerical schemes and a more thorough treatment of the solid wall boundary conditions are deferred for future study. Second, with the exception of the Re = 100 cases, the vortex locations are relatively insensitive to the choice of pressure evolution scheme (AC or EDAC) as well as the chosen Mach number, although some error is seen at Ma = 0.3. The value of the stream function shows only slightly more sensitivity. Again, while some small deviations from the high-resolution numerical results of Ghia *et al.* [30] and Erturk *et al.* [31] are seen, the deviations between the AC and EDAC methods are small, which suggests that the general numerical scheme is causing these deviations, and not the choice of the pressure evolution equation.

TABLE II. Location of tertiary vortex at Re = 5000.

Simulation	Vortex location (x, y, $\psi \times 10^3$)
Ghia *et al.* [30]	(0.0625, 0.9102, −1.4564)
Hou *et al.* [33]	(0.0667, 0.9059, −1.40)
Borok *et al.* [22], Ma = 0.05	(0.0667, 0.9137, −1.45)
AC, Ma = 0.1	(0.0627, 0.9098, −1.3887)
EDAC, Ma = 0.1	(0.0627, 0.9098, −1.3926)
EDAC, Ma = 0.3	(0.0627, 0.9098, −1.4932)

TABLE I. Location of primary and secondary vortices for LDCF simulations.

Simulation	Primary vortex (x, y, ψ)	Bottom left vortex (x, y, $\psi \times 10^5$)	Bottom right vortex (x, y, $\psi \times 10^4$)
Re = 100			
Ghia *et al.* [30]	(0.6172, 0.7344, 0.10342)	(0.0313, 0.0391, −0.17488)	(0.9453, 0.0625, −0.12537)
Hou *et al.* [33]	(0.6196, 0.7373, 0.1030)	(0.0392, 0.0353, −0.172)	(0.9451, 0.0627, −0.122)
AC, Ma = 0.1	(0.6157, 0.7373, 0.10320)	N/A	(0.9451, 0.0628, 0.35492)
EDAC, Ma = 0.1	(0.6157, 0.7373, 0.10294)	(0.0549, 0.0157, −1.5972)	(0.9451, 0.0628, −0.28197)
EDAC, Ma = 0.3	(0.6157, 0.7412, 0.10145)	(0.0196, 0.0980, −36.418)	(0.9412, 0.0588, −1.0248)
Re = 1000			
Ghia *et al.* [30]	(0.5313, 0.5625, 0.11793)	(0.0859, 0.0781, −23.113)	(0.8594, 0.1094, −17.510)
Hou *et al.* [33]	(0.5333, 0.5647, 0.1178)	(0.0902, 0.0784, −22.2)	(0.8667, 0.1137, −16.9)
Erturk *et al.* [31]	(0.5300, 0.5650, 0.11878)	(0.0833, 0.0783, −23.261)	(0.8633, 0.1117, −17.281)
Borok *et al.* [22], Ma = 0.01	(0.5373, 0.5686, 0.1175)	(0.0863, 0.0784, −21)	(0.8667, 0.1137, −18.5)
AC, Ma = 0.1	(0.5294, 0.5647, 0.11810)	(0.0863, 0.0745, −18.585)	(0.8627, 0.1137, −17.189)
EDAC, Ma = 0.1	(0.5294, 0.5647, 0.11800)	(0.0824, 0.0784, −18.851)	(0.8627, 0.1137, −17.243)
EDAC, Ma = 0.3	(0.5294, 0.5647, 0.11704)	(0.0745, 0.0823, −16.857)	(0.8627, 0.1137, −16.860)
Re = 5000			
Ghia *et al.* [30]	(0.5117, 0.5352, 0.11897)	(0.0703, 0.1367, −136.12)	(0.8086, 0.0742, −30.836)
Hou *et al.* [33]	(0.5176, 0.5373, 0.1214)	(0.0784, 0.1373, −135)	(0.8078, 0.0745, −30.3)
Erturk *et al.* [31]	(0.5150, 0.5350, 0.12129)	(0.0733, 0.1367, −136.39)	(0.8050, 0.0733, −30.604)
Borok *et al.* [22], Ma = 0.05	(0.5176, 0.5451, 0.1107)	(0.0784, 0.1333, −107)	(0.7922, 0.0824, −32.6)
AC, Ma = 0.1	(0.5137, 0.5373, 0.11943)	(0.0745, 0.1333, −117.07)	(0.7961, 0.0706, −32.870)
EDAC, Ma = 0.1	(0.5137, 0.5373, 0.11935)	(0.0745, 0.1333, −116.58)	(0.7961, 0.0706, −32.850)
EDAC, Ma = 0.3	(0.5137, 0.5373, 0.11863)	(0.0706, 0.1373, −106.36)	(0.7922, 0.0706, −30.371)

B. Traveling wave

To explore the transient behavior of the EDAC method, the traveling-wave solution given in Eqs. (22)–(24) is used. This equation is an exact solution to the INS for a convecting, decaying Taylor-Green vortex. It is important to note that the solution in Eqs. (22)–(24) at $t = 0$ is not an exact solution to either the AC or EDAC methods, thus an initial perturbation is introduced that must decay, and the smoothing term that appears in Eq. (12) is crucial to recover time-accurate dynamics at moderate values of the Mach number. Traditional AC schemes must use an extremely small Mach number in order to keep the pressure fluctuations from polluting the solution domain. The error in the traditional AC method is magnified at very low Reynolds numbers. Since literature results were not available for solutions to this problem using the LB method, a simple two-dimensional nine-direction LB model is used for comparisons. A single-relaxation-time model is used, where the relaxation time is given by τ. Further details involving the theory and implementation of the LB method are outside the scope of this paper and can be found in Aidun and Clausen [19].

While the KRLNS method showed errors in the steady-state solution of the LDCF problem, the solution of the traveling-wave problem reveals a qualitatively incorrect evolution of the pressure field. To illustrate this error, simulations are performed on a 65×65 domain at $\mathrm{Re} = 1$ with periodic boundary conditions and $\Delta t = 2.96 \times 10^{-5}$. In Fig. 6(a), one can see that a naive implementation of the reduced KRLNS equations listed in Borok *et al.* [22] results in a pressure decay that is much too rapid, and an incorrect steady pressure after the complete decay of the vortex. The error is still present as the Mach number is reduced. Upon addition of $\frac{1}{\mathrm{Re}}\nabla \boldsymbol{u} : \nabla \boldsymbol{u}$ from Eq. (16), the KRLNS results converge to those of the EDAC, demonstrating that this term is largely responsible for the incorrect results. The EDAC results agree well with the analytical curve. Figure 6(b) shows the divergence errors associated with the methods. Again, the largest divergence errors are seen with the unmodified KRLNS method. While this divergence error does decrease with decreasing Mach number, the corrected KRLNS and EDAC methods show very small divergence errors even at the larger $\mathrm{Ma} = 0.1$. The errors in the pressure and velocity divergence are much more pronounced than the velocity component errors, which are not shown for these cases. Since the KRLNS method neglects a term important for low-Reynolds-number flow, the remainder of this paper will focus on characterizing the EDAC method in comparison with the AC and LB methods.

The previous experiment is repeated using the AC, LB, and EDAC methods, and the results are shown in Fig. 7. The same number of grid points and time step size are used, except for the LB method where $\Delta t = 8.88 \times 10^{-5}$. The LB simulation uses a relaxation time of $\tau = 1.62$. The traditional AC method and the LB method both show oscillations in the solution. The pressure oscillations are more pronounced in the AC method than the LB method; however, both methods show similar velocity-divergence errors. At high-Mach numbers, the physical relevance of the AC method is lost. Increasing the Mach number in LB simulations at a fixed Reynolds number requires increasing τ, which causes a degradation in the solution accuracy, particularly for the single-relaxation-time model used here; thus, LB simulations are limited to $\mathrm{Ma} = 0.01$. In contrast to the AC and LB methods, the EDAC method shows little error. Essentially, no pressure oscillations are seen and the thermodynamic formulation associated with the EDAC method results in much smaller divergence errors than the other methods.

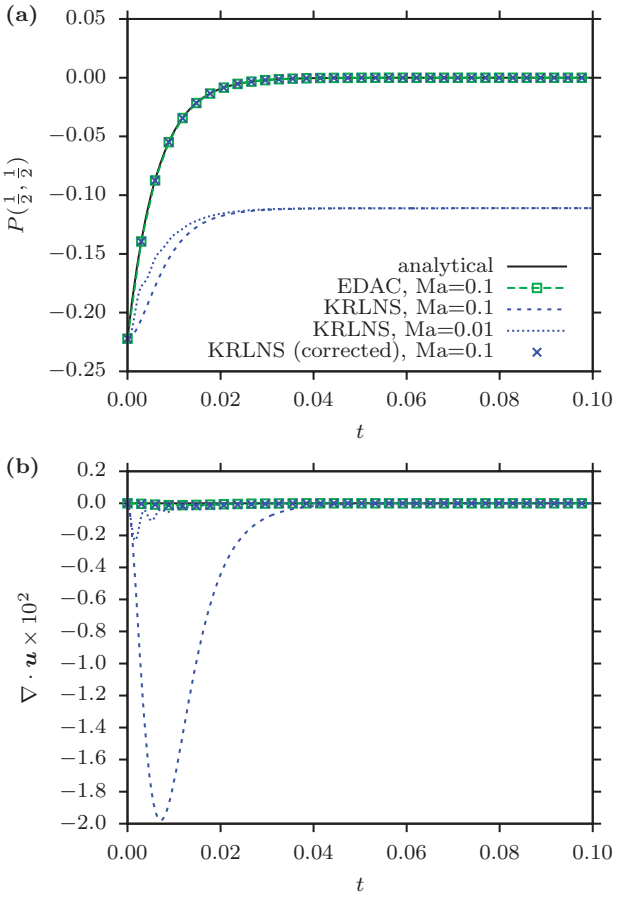

FIG. 6. (Color online) Traveling-wave solution showing the (a) pressure and (b) velocity divergence at location (1/2,1/2) at $\mathrm{Re} = 1$. The KRLNS method error creates qualitatively incorrect behavior unless a correction term is included.

When using a strictly explicit scheme, there is little reason to increase the Mach number beyond 0.01 at $\mathrm{Re} = 1.0$, since the time step size is diffusion limited; however, mixed implicit-explicit schemes are a possibility. Furthermore, the poor behavior of the AC method at $\mathrm{Ma} = 0.1$, which is still approximately incompressible, demonstrates that the underlying physics associated with the AC method are not generally applicable for transient simulations at all Re. These limitations are not present with the EDAC method. Another issue exists in the pressure-mode coupling and the lack of smoothing associated with using collocated pressure and velocity variables, i.e., a nonstaggered grid. In previous investigations [16], the solution of the AC method on a staggered grid was found to demonstrate similar pressure fluctuations as the LB method, although some investigators have used AC on nonstaggered grids [17]. The ability of the EDAC method to use a simpler collocated scheme is beneficial and results in simpler algorithms.

As the Reynolds number increases, the relative importance of the pressure smoothing term is decreased. Nonetheless, the

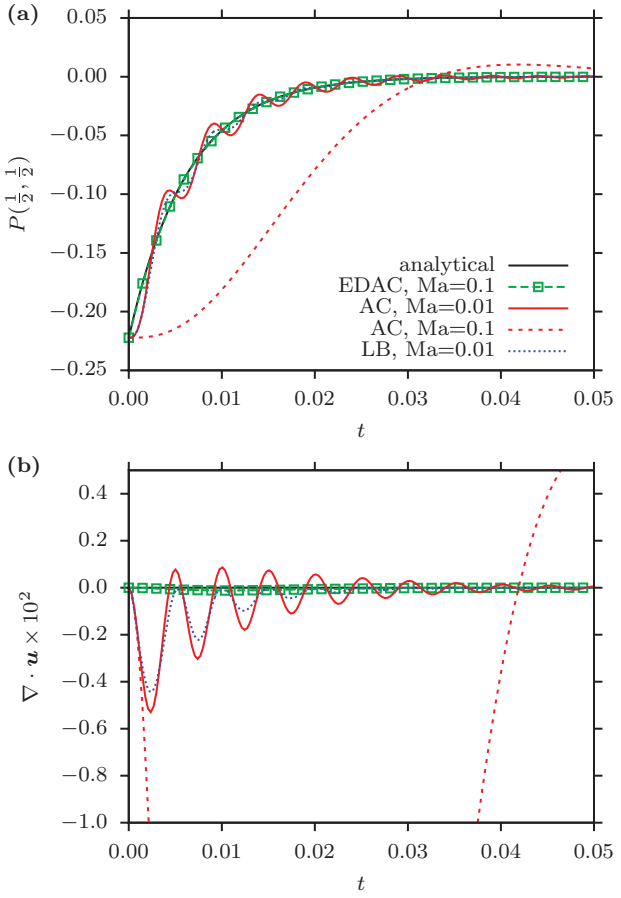

FIG. 7. (Color online) Traveling-wave solution showing the (a) pressure and (b) velocity divergence at location (1/2,1/2) at Re = 1. Pressure and velocity-divergence errors exist for the AC and LB methods. The EDAC method rapidly damps the fluctuations showing greatly reduced errors.

smoothing introduced in the EDAC method results in improved behavior. Figure 8 shows the results for a simulation domain of 65×65 and $\mathrm{Re} = 1000$. The time step is 4.77×10^{-4} for the $\mathrm{Ma} = 0.1$ AC and EDAC cases, 8.89×10^{-4} for the LB case, and 5.36343×10^{-5} for the $\mathrm{Ma} = 0.01$ AC case. Figure 8(a) shows the pressure, with generally good results seen for all methods, although some oscillations still exist as seen in the zoomed region shown by Fig. 8(b). Looking at the divergence errors shows that the EDAC method consistently outperforms the traditional AC method, with divergence errors on the same magnitude as the LB method.

C. Doubly periodic shear layer

A doubly periodic shear layer is also considered. In this problem, a periodic domain of $[1 \times 1]$ is considered, with a uniform pressure field and velocity initial conditions of

$$u(x,y) = \begin{cases} \tanh[\delta_w(y-0.25)] & \text{if} \quad y \leqslant 0.5, \\ \tanh[\delta_w(0.75-y)] & \text{if} \quad y > 0.5, \end{cases} \tag{25}$$

$$v(x,y) = \delta_p \sin[2\pi(x+0.25)], \tag{26}$$

where δ_w is a parameter governing the width of the shear layer and δ_p is the strength of the initial perturbation. In this system,

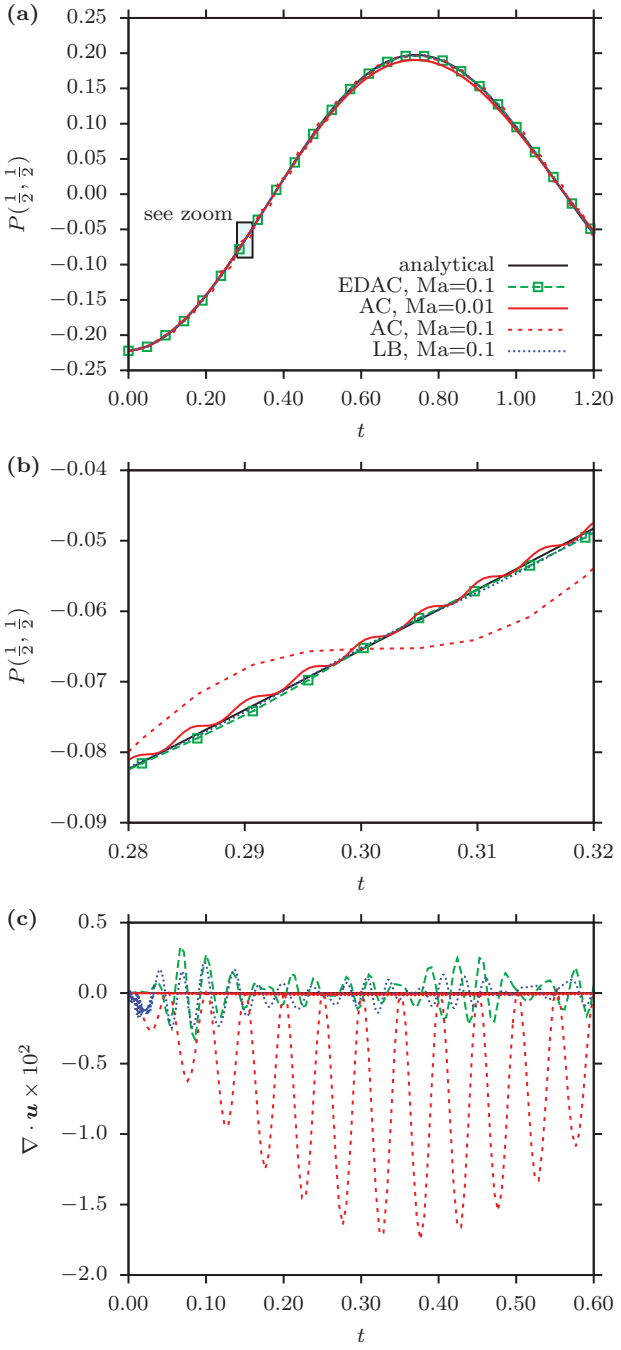

FIG. 8. (Color online) Traveling-wave solution showing the (a) pressure and (b) velocity divergence at location (1/2,1/2) at Re = 1000. Pressure and velocity-divergence errors exist for the AC and LB methods. The EDAC method rapidly damps the fluctuations showing greatly reduced errors.

first investigated by Bell *et al.* [34] and studied in depth by Minion and Brown [27], the shear layers roll up into a pair of symmetric vortices. In cases in which the mesh is too coarse relative to the thickness of the shear layers, spurious vortices are created. All of the cases considered here use $\delta_w = 80$ and $\delta_p = 0.05$, which corresponds to the thin shear-layer cases in Minion and Brown [27]. The Reynolds number is 10 000. Figure 9 shows the vorticity at a time $t = 1$ for mesh sizes of (a) 128×128 and (b) 256×256 for the EDAC method.

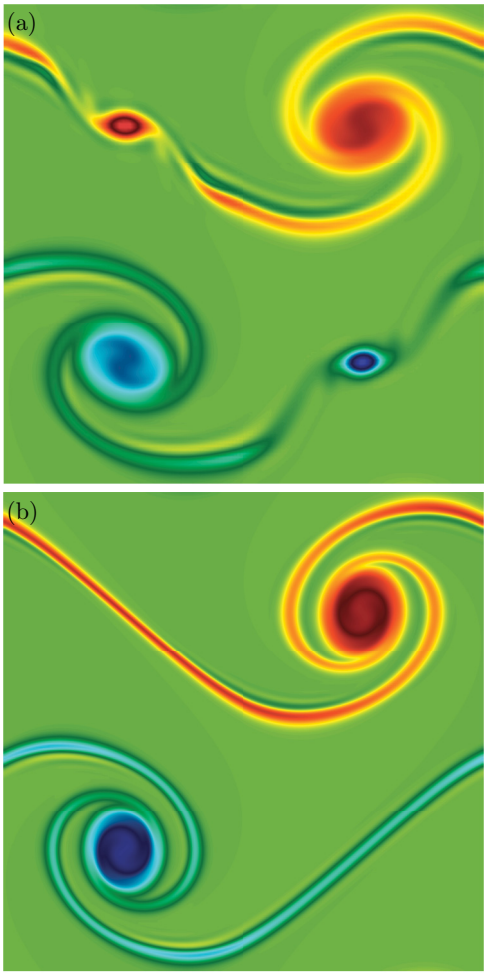

FIG. 9. (Color online) Doubly periodic shear-layer test using the EDAC method showing the vorticity at $t = 1$ for meshes of (a) 128×128 and (b) 256×256.

In the coarse mesh case, the spurious vortices are clearly present, while in the refined case, the vortices have been suppressed. Simulations using traditional AC or LB techniques (not shown) also show similar behavior, which is consistent with literature results [27] in which spurious vortices were seen on under-resolved meshes regardless of the underlying numerical method.

Next, the global enstrophy Ω and energy E are calculated according to

$$\Omega = \sum_{i=1}^{N} \frac{\omega_i^2 A_i}{2A}, \tag{27}$$

$$E = \sum_{i=1}^{N} \frac{(\boldsymbol{u} \cdot \boldsymbol{u}) A_i}{2A}, \tag{28}$$

where the summation is over the number of nodes N, ω is the vorticity, A_i is the cell area, and A is the overall domain area. The vorticity is calculated using a fourth-order central difference. The enstrophy and energy decays are shown in Fig. 10 for the EDAC and AC methods at several grid sizes. Also shown are pseudospectral (Pspect), pressure-Poisson (PPois), Godunov projection (GProj), and upwind velocity–stream-function (VSup) [27] methods. The pseudospectral results are performed on a 768×768 grid, while the pressure-Poisson, Godunov projection, and velocity–stream-function results are performed on a 128×128 grid. The pseudospectral and pressure-Poisson results are shown to have fourth-order convergence, while the upwind velocity–stream-function and Godunov projection results show second-order convergence.

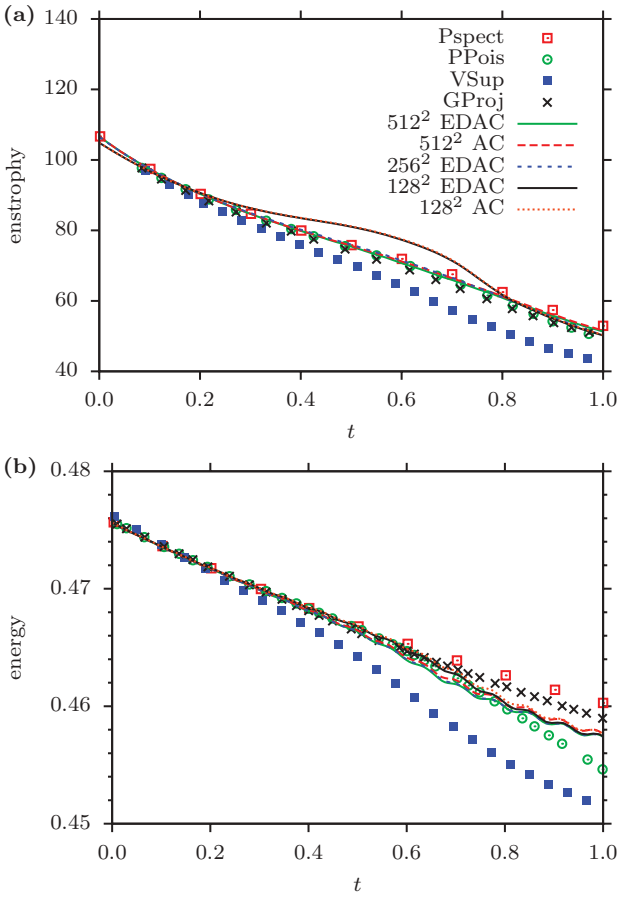

FIG. 10. (Color online) Enstrophy and energy decay for a pseudospectral (Pspect) reference solution, pressure-Poisson (PPois), and upwind vorticity–stream-function (VSup), as well as the EDAC and AC methods. Ma = 0.1 for all EDAC and AC methods.

For the enstrophy decay, the coarse grid simulation shows some deviation from the reference solution (Pspect). The deviations are likely caused by insufficient resolution to resolve the thin shear layer, where all the enstrophy is located. For the under-resolved 128^2 cases, the choice of finite-difference stencil for the vorticity calculation can alter the enstrophy results significantly. Longer term deviations could be attributed to the formation of spurious vortices at this mesh resolution. With higher mesh resolutions, the shear layer is captured and spurious vortices do not form, and both the AC and EDAC methods compare well with the pseudospectral method. For the energy case, all EDAC and AC methods, while slightly more dissipative than the pseudospectral method and Godunov projection methods, perform well and demonstrate less dissipation than the pressure-Poisson and vorticity–stream-function results. Some oscillations are seen in the solution associated with oscillations due to acoustic waves. At this high Reynolds number (Re = 10 000), additional dissipation

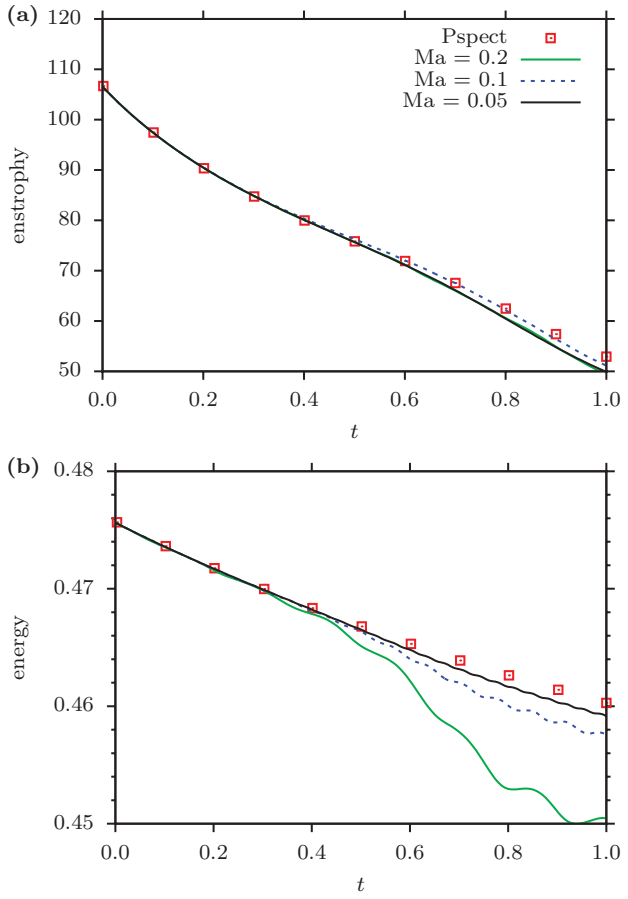

FIG. 11. (Color online) Effect of Mach number on enstrophy and energy decay for the EDAC method on a 256 × 256 grid.

in the EDAC method is minimal, thus EDAC and AC methods appear nearly identical in behavior.

In Fig. 11, the effect of the Ma number is explored for the EDAC method, with a mesh size of 256 × 256 for all simulations. Enstrophy results are relatively insensitive to the selection of Ma number; however, the energy decay shows a strong sensitivity to the Mach number. At Ma = 0.2, the simulation is much too dissipative, and fluctuations are clearly present that are associated with the finite speed of the acoustic waves. At the smallest Mach number (Ma = 0.5), the EDAC method compares favorably with the pseudospectral method.

V. CONCLUSIONS

In this paper, an alternative to the standard AC technique is presented. Unlike the method devised by Chorin [11], in which the artificial equation of state enforces isentropic behavior, the alternative method, called EDAC, uses a thermodynamic relationship which creates entropy to damp the acoustic pressure waves. The development of the EDAC method follows the recently published KRLNS method [20–22], in which a damping term is shown to be beneficial. In contrast to the KRLNS method, the development of the EDAC method forgoes the substitution for the grand potential, and instead proceeds directly from the CNS in a simple fashion. Through this derivation, the EDAC equations result from the addition of a constraint that minimizes density fluctuations instead of enforcing isentropic behavior. The same relationship is assumed in the derivation of the KRLNS, but this relationship is not explicitly stated as an additional and artificial constraint on the system. Furthermore, the simplified EDAC equations reveal that a term is incorrectly neglected in the reduced KRLNS equations [22], which yields qualitatively incorrect behavior as seen in the traveling-wave problem.

The AC, EDAC, and KRLNS methods are discretized using a simple MacCormack finite-difference scheme for the purposes of this investigation. A small verification test is performed, and then the various methods are compared using steady lid-driven cavity and transient traveling-wave tests. As is known, the traditional AC method shows fluctuations associated with the propagation of acoustic waves, which creates errors in the pressure and velocity divergence. The errors in the AC method are particularly evident at low Reynolds numbers, whereas the EDAC method effectively damps these oscillations. Both the AC and EDAC methods converge to the INS in the limit Ma → 0; however, differences exist in terms of $O(\mathrm{Ma}^2)$. As Re → ∞, fluid behavior naturally becomes isentropic, and the AC and EDAC methods converge. In contrast to the traditional AC method, the EDAC method is consistent in the limit Re → 0, since the pressure evolution becomes the pressure-Poisson equation for a Stokes fluid.

Renewed interest in the general class of pseudocompressible methods, i.e., methods in which the flow is allowed to have a small but finite level of compressibility, is motivated by the ability of these methods to operate in a fully explicit manner when simulating (nearly) incompressible flows, avoiding the necessarily implicit pressure-Poisson solve. Fully explicit methods involve local communication, which can be trivially scaled on emerging massively parallel architectures and GPGPU computing. This massively parallel capability has been one of the reasons that the LB method, also a pseudocompressible method, has become popular for certain types of simulations. Unlike the LB method, the AC and EDAC methods remain based on continuum conservation laws, which alleviates difficulties in formulating more complex boundary conditions and constitutive models.

Despite their attractiveness, fully explicit methods have significant limitations, namely, the time step limitations due to diffusion, acoustic wave propagation, and convection. As such, these methods excel in transient simulations where time accuracy requires time steps on the order of the stability limits. Beyond using the EDAC method in a strictly explicit setting, the EDAC method provides a natural and physically motivated mechanism to relax the high-frequency errors in the pressure field. When combined with multigrid techniques [35] to relax the low-frequency errors, the EDAC scheme may become attractive for relaxing to a steady solution, although more investigation is required and will be a focus of future effort.

ACKNOWLEDGMENTS

Sandia National Laboratories is a multiprogram laboratory managed and operated by Sandia Corporation, a wholly owned subsidiary of Lockheed Martin Corporation, for the US Department of Energy's National Nuclear Security Administration under Contract No. DE-AC04-94AL85000.

APPENDIX: METHOD OF MANUFACTURED SOLUTION SOURCE TERMS

The method of manufactured solutions provides a way to isolate discretization error in numerical methods. For the AC (8) and EDAC (12) pressure evolution equations, a source term can be added to the right-hand side that makes the traveling-wave solution given in Eqs. (22)–(24) exact. The source terms are listed as

$$S_{\mathrm{EDAC}} = \frac{8\pi}{27} e^{-24\pi^2 t/\mathrm{Re}} \left\{ \cos\left[4\pi\left(-\frac{t}{3}+x\right)\right] - \cos\left[4\pi\left(-\frac{t}{3}+y\right)\right] \right\} \sin\left[2\pi\left(-\frac{t}{3}+x\right)\right] \sin\left[2\pi\left(-\frac{t}{3}+y\right)\right], \tag{A1}$$

and

$$\begin{aligned} S_{\mathrm{AC}} = {} & \frac{16\pi^2}{9\mathrm{Re}} e^{-16\pi^2 t/\mathrm{Re}} \left\{ \cos\left[4\pi\left(-\frac{t}{3}+x\right)\right] + \cos\left[4\pi\left(-\frac{t}{3}+y\right)\right] \right\} \\ & - \frac{1}{9} e^{-16\pi^2 t/\mathrm{Re}} \left\{ \frac{4}{3}\pi \sin\left[4\pi\left(-\frac{t}{3}+x\right)\right] + \frac{4}{3}\pi \sin\left[4\pi\left(-\frac{t}{3}+y\right)\right] \right\}, \end{aligned} \tag{A2}$$

for the EDAC and AC methods, respectively.

[1] S. Paolucci, Sandia National Laboratories Technical Report No. SAND-82-8257, 1982, www.ntis.gov.
[2] A. J. Chorin, Math. Comp. **22**, 745 (1968).
[3] A. J. Chorin, Math. Comp. **23**, 341 (1969).
[4] S. Patankar and D. Spalding, Int. J. Heat Mass Transfer **15**, 1787 (1972).
[5] R. Issa, J. Comput. Phys. **62**, 40 (1986).
[6] A. S. Almgren, J. B. Bell, and W. G. Szymczak, SIAM J. Sci. Comput. **17**, 358 (1996).
[7] M. L. Minion, J. Comput. Phys. **127**, 158 (1996).
[8] D. L. Brown, R. Cortez, and M. L. Minion, J. Comput. Phys. **168**, 464 (2001).
[9] "ASC Sequoia", https://asc.llnl.gov/computing_resources/sequoia/ (unpublished).
[10] R. R. R. Bordawekar and U. Bondhugula, IBM T. J. Watson Research Center Technical Report No. RC25033 (W1008-020), 2010 [www.research.ibm.com] (unpublished).
[11] A. J. Chorin, J. Comput. Phys. **2**, 12 (1967).
[12] C. L. Merkle and M. Athavale, in *Proceedings of the Eighth Computational Fluid Dynamics Conference, AIAA Paper 87–1137, Honolulu, HI* (AIAA, 1987), pp. 397–407 [www.aiaa.org].
[13] S. E. Rogers, D. Kwak, and C. Kiris, AIAA J. **29**, 603 (1991).
[14] C. Kiris and D. Kwak, Comput. Fluids **31**, 627 (2002).
[15] R. R. Nourgaliev, T. N. Dinh, and T. G. Theofanous, Int. J. Multiphase Flow **30**, 901 (2004).
[16] X. He, G. Doolen, and T. Clark, J. Comput. Phys. **179**, 439 (2002).
[17] A. Perrin and H. H. Hu, J. Comput. Phys. **212**, 166 (2006).
[18] S. Chen and G. D. Doolen, Annu. Rev. Fluid Mech. **30**, 329 (1998).
[19] C. K. Aidun and J. R. Clausen, Annu. Rev. Fluid Mech. **42**, 439 (2010).
[20] S. Ansumali, I. V. Karlin, and H. C. Ottinger, Phys. Rev. Lett. **94**, 080602 (2005).
[21] I. V. Karlin, A. G. Tomboulides, C. E. Frouzakis, and S. Ansumali, Phys. Rev. E **74**, 035702 (2006).
[22] S. Borok, S. Ansumali, and I. V. Karlin, Phys. Rev. E **76**, 066704 (2007).
[23] R. Panton, *Incompressible Flow* (Wiley-IEEE, New York, 1996).
[24] R. W. MacCormack, in *Hypervelocity Impact Conference, AIAA Paper 69–354, Cincinnati, OH* (AIAA, 1969) [www.aiaa.org].
[25] J. C. Tannehill, D. A. Anderson, and R. H. Pletcher, *Computational Fluid Mechanics and Heat Transfer* (Taylor & Francis, Washington, DC, 1997).
[26] P. J. Roache, J. Fluids Eng. **124**, 4 (2002).
[27] M. Minion and D. Brown, J. Comput. Phys. **138**, 734 (1997).
[28] C. K. Aidun, Y. Lu, and E. J. Ding, J. Fluid Mech. **373**, 287 (1998).
[29] J. R. Clausen, D. A. Reasor, and C. K. Aidun, Comput. Phys. Commun. **181**, 1013 (2010).
[30] U. Ghia, K. N. Ghia, and C. T. Shin, J. Comput. Phys. **48**, 387 (1982).
[31] E. Erturk, T. C. Corke, and C. Gökçöl, Int. J. Numer. Meth. Fluids **48**, 747 (2005).
[32] E. Hachem, B. Rivaux, T. Kloczko, H. Digonnet, and T. Coupez, J. Comput. Phys. **229**, 8643 (2010).
[33] S. Hou, Q. Zou, S. Chen, G. Doolen, and A. C. Cogley, J. Comput. Phys. **118**, 329 (1995).
[34] J. B. Bell, P. Colella, and H. M. Glaz, J. Comput. Phys. **85**, 257 (1989).
[35] A. Jameson, Appl. Math. Comput. **13**, 327 (1983).